Structural Analysis of B-Box 2 from MuRF1: Identification of a Novel Self-Association Pattern in a RING-like Fold[†,‡]

Michael Mrosek,[§] Sebastian Meier,[§,||] Zöhre Ucurum-Fotiadis,[§,||] Eleonore von Castelmur,[§] Erik Hedbom,[§] Ariel Lustig,[§] Stephan Grzesiek,[§] Dietmar Labeit,[⊥] Siegfried Labeit,[⊥] and Olga Mayans*[,§,@]

Division of Structural Biology, Biozentrum, University of Basel, Klingelbergstrasse 70, CH-4056 Basel, Switzerland, Institut für Anästhesiologie and Operative Intensivmedizin, Universitätsklinikum Mannheim, D-68167 Mannheim, Germany, and School of Biological Sciences, University of Liverpool, Crown Street, Liverpool L69 7ZB, U.K.

Received April 24, 2008; Revised Manuscript Received July 31, 2008

ABSTRACT: The B-box motif is the defining feature of the TRIM family of proteins, characterized by a RING finger−B-box−coiled coil tripartite fold. We have elucidated the crystal structure of B-box 2 (B2) from MuRF1, a TRIM protein that supports a wide variety of protein interactions in the sarcomere and regulates the trophic state of striated muscle tissue. MuRF1 B2 coordinates two zinc ions through a cross-brace α/β-topology typical of members of the RING finger superfamily. However, it self-associates into dimers with high affinity. The dimerization pattern is mediated by the helical component of this fold and is unique among RING-like folds. This B2 reveals a long shallow groove that encircles the C-terminal metal binding site ZnII and appears as the defining protein−protein interaction feature of this domain. A cluster of conserved hydrophobic residues in this groove and, in particular, a highly conserved aromatic residue (Y133 in MuRF1 B2) is likely to be central to this role. We expect these findings to aid the future exploration of the cellular function and therapeutic potential of MuRF1.

Zinc-binding motifs play key physiological and structural roles in a broad range of proteins, including storage and structural proteins, enzymes, and transcription factors. The "B-box" is a small zinc-binding domain (∼40 residues) found exclusively in eukaryotes. It occurs within the context of a tripartite fold known as TRIM[1] (*1*−*3*), which consists of up to three sequentially conserved zinc-binding domains [commonly a RING finger, a B-box type 1 (B1), and a B-box type 2 (B2)] followed by a coiled coil fraction (CC). In those cases where a single B-box is present, it is usually of type B2. The presence of a B-box is the determinant of the TRIM fold, since it is found only in members of this family.

TRIM proteins have been attributed roles in the regulation of gene expression, cell growth, and differentiation, thereby being associated with human proliferative pathologies [e.g., cancer, familiar Mediterranean fever, Opitz/BBB syndrome, promyelocytic leukemia, mulibrey nanism, and thyroid carcinomas (*4*)]. Accumulating evidence suggests that B-boxes mediate protein−protein interactions specific to each TRIM class (e.g., refs *5*−*7*) and are crucial for the efficient self-assembly of this fold (*3* and references therein). Recently, atomic structures of B1 and B2 boxes have become available, namely, the B1 boxes of MID1 (*8*) and TRIM19 (PDB entry 2D8V) and the B2 boxes of ATDC (2CSV), TRIM39 (2DID), TRIM41 (2EGM), TRIM5 (2YRG), MuRF1 (2D8U), MID2 (2DJA), and MID1 (*9*). These structures reveal that the B-box fold exhibits a $\beta\beta\alpha$ RING-like architecture that coordinates two zinc ions in a classical "cross-brace" topology, where zinc-binding site I (ZnI) is formed by the first and third ligand pairs and zinc-binding site II (ZnII) by the second and fourth ligand sets. The recent B-box models differ significantly from a structure previously described for B2 of *Xenopus* XNF7 (*10*), which adopted a topology unique among zinc-binding folds and coordinated one single zinc ion leaving four potential metal ligands unoccupied. For more than a decade, the fold of XNF7 B2 was thought to represent the canonical B-box motif. However, it is now evident that that model, calculated from a refolded synthetic peptide, does not represent a physiologically relevant fold.

To further investigate the characteristics of the B2 motif, we have analyzed the structure and self-association properties of the B2 from the ubiquitin ligase MuRF1 using X-ray crystallography, NMR spectroscopy, light scattering, and analytical ultracentrifugation. MuRF1 contains a RING domain in the N-terminal position, a specific MuRF family domain (MFC), a single B2 box, a CC domain, and a C-terminal acidic tail (Figure 1). We selected MuRF1 for our studies since it contributes to the control of the trophic state of cardiac and skeletal muscle and its inactivation can slow the development of muscle atrophy (*11, 12*). MuRF1 interacts with an intriguingly wide variety of cellular partners,

[†] This work was supported by grants from The Royal Society to O.M. and DFG (La668/11-1) to S.L. M.M. and Z.U.-F. were supported by SNF (3100A0-100852).

[‡] Atomic coordinates and experimental structure factor amplitudes have been deposited in the Protein Data Bank as entry 3DDT.

* To whom correspondence should be addressed. Telephone: +44 (0)151 7954472. Fax: +44 (0)151 7954406. E-mail: Olga.Mayans@liverpool.ac.uk.

[§] University of Basel.

[||] These authors contributed equally to this work.

[⊥] Universitätsklinikum Mannheim.

[@] University of Liverpool.

[1] Abbreviations: B2, B-box type 2; CC, coiled coil; MuRF, muscle-specific RING finger; TRIM, tripartite motif.

10.1021/bi800733z CCC: $40.75
Published on Web 09/17/2008

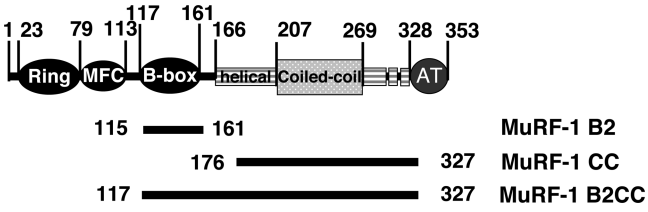

FIGURE 1: Domain structure of MuRF1. MFC refers to a MuRF family specific motif, and AT denotes the C-terminal acidic tail. The residue composition of the protein constructs used in this study is indicated.

namely, the titin filament (*13, 14*), isopeptidase T-3 (*15*), the transcription regulator GMEB-1 (*15*), CARP, SQSTM1, and EEF1G (*12*). Further, MuRF1 also participates in sumoylation pathways (*13, 15*). Although the specific motifs in the multidomain MuRF1 that are responsible for these interactions are still unknown, its B2 box has recently been shown to participate in the binding of creatine kinase (*16*), providing a further link between myofibril turnover and muscle metabolism. Our data show that MuRF1 B2 presents a distinct dimerization pattern and allow us to propose sequence and surface features that might sustain the protein interactions mediated by this motif, aiding future studies of its cellular role and potential therapeutic targeting.

EXPERIMENTAL PROCEDURES

Cloning. Truncated variants of human MuRF1 (Q969Q1) (Figure 1) were cloned into vector pETM-11 (EMBL collection) containing an N-terminal His_6 tag and a TEV protease cleavage site prior to the target gene. The $B2^{C137D}$ variant was engineered in pETM-11 using the QuikChange protocol (Stratagene). The B2CC construct corresponded to a C293S variant designed to prevent sample oxidation.

Protein Production. Expression occurred in *Escherichia coli* BL21(DE3) Rosetta (Novagen). Cultures were grown at 37 °C to an OD_{600} of 0.6 in Luria-Bertani medium supplemented with 25 μg/mL kanamycin and 34 μg/mL chloramphenicol. Expression was induced with 0.2−0.5 mM IPTG, and cultures were grown for a further 18 h at 20−25 °C. To obtain soluble B2 and B2CC samples, media were supplemented with 50 μM $ZnCl_2$ upon induction. Harvesting was accomplished via centrifugation. Pellets were resuspended in 50 mM Tris (pH 8.0), 100 mM NaCl, and 10 mM β-mercaptoethanol containing a protease inhibitor cocktail (Roche). Lysis was by addition of lysozyme and French pressing in the presence of DNase. The homogenate was clarified by centrifugation and the supernatant applied to a Ni^{2+}-chelating HisTrap column (GE Healthcare) equilibrated in lysis buffer containing 20 mM imidazole. Elution used 250 mM imidazole. The eluate was dialyzed against 50 mM Tris (pH 8.0), 150 mM NaCl, and 10 mM β-mercaptoethanol in the presence of His-tagged TEV protease at 4 °C overnight. Subsequent purification involved reverse affinity chromatography on a HisTrap column followed by gel filtration on a Superdex 75 16/60PG column (GE Healthcare) equilibrated in lysis buffer. Pure samples were concentrated to 10 mg/mL (BCA assay, Pierce) and stored until further use.

Expression of $B2^{C137D}$ according to the protocol described above resulted in insoluble sample, possibly reflecting a decrease in zinc affinity. Consequently, the bacterial pellet was resuspended in lysis buffer supplemented with 8 M urea and subjected to affinity purification under denaturing conditions. Eluted fractions were dialyzed overnight against a refolding buffer containing 50 mM Tris (pH 8.0), 150 mM NaCl, 10 mM β-mercaptoethanol, and 1 mM $ZnCl_2$. The refolded sample was processed further as the wild type.

Table 1: Experimental Diffusion Parameters for MuRF-1 B2 from ^{15}N Relaxation Data[a]

model	$\tau_{c,eff}$[b] (ns)
isotropic	6.39
axially symmetric	6.39
fully asymmetric	6.40

[a] At 25 °C in water. [b] $\tau_{c,eff}$ is calculated from $(6D)^{-1}$, where $D = (D_x + D_y + D_z)/3$; rotational diffusion was analyzed with TENSOR (*25*).

Crystal Structure Elucidation. Crystals grew from solutions containing 1.8 M ammonium sulfate, 0.1 M Tris (pH 8.5), and 15% glycerol at 4 °C in hanging drops composed of a 1:1 ratio of protein and reservoir solutions. Hexagonal crystals with dimensions of ~200 μm × 200 μm × 100 μm grew within 2 days, typically showing visible macrotwinning. X-ray data were collected from a selected single crystal frozen at 100 K in native mother liquor. Data processing used the XDS package (*17*) (statistics given in Table 2). Phasing was carried out using a 3λ MAD experiment that exploited the signal from endogenous zinc ions. The location of anomalous scatterers and phase calculation were conducted with SOLVE (*18*), while density modification and initial model building were conducted in RESOLVE (*19*). Further automated building used ARP/wARP (*20*). Manual model editing was conducted in O (*21*) and final refinement in PHENIX (*22*). The final model contains all protein residues with the exception of C-terminal residue S161 in chains B and C that was not visible in electron density maps.

Crystals of $B2^{C137D}$ grew from 1.8 M ammonium sulfate, 0.1 M Tris (pH 8.5), and 5% glycerol at 18 °C (protein concentration like that of the wild type). X-ray data were collected on an Elliot GX20 rotating anode up to 3.4 Å resolution. Crystals belonged to space group $P2_12_12_1$ with six B-box protomers (three biological dimers) per asymmetric unit and the following cell dimensions: $a = 60.77$ Å, $b = 66.80$ Å, and $c = 77.40$ Å. Lattice reconstruction was by molecular replacement in PHASER (*23*) using the wild-type monomer lacking zinc ions as a search model. Map calculation was preceded by mild refinement.

Analytical Ultracentrifugation. Sedimentation equilibrium data were recorded using an Optima XL-A analytical ultracentrifuge (Beckman Instruments) equipped with 4 and 12 mm Epon double-sector cells in an An-60 Ti rotor and absorption optics. Runs were performed at 20 °C in 50 mM Tris (pH 8.0) and 150 mM NaCl at 24000, 28000, and 34000 rpm and protein concentrations of 0.025−0.4 mg/mL, where OD values remained linear. A detection wavelength of 232 nm was used because of the low extinction coefficient of the sample. Average molecular masses were evaluated using SEGAL (*24*). A protein partial specific volume of 0.73 mL/g was employed, while the solution density was taken to be 1.003 g/mL and the viscosity to be 1.02 cP.

NMR Experiments. ^{15}N-labeled B2 was expressed in M9 minimal medium using $^{15}NH_4Cl$ as the nitrogen source and

Table 2: X-ray Data and Model Refinement Statistics

		MAD (six zinc atoms)		
		peak	inflection	remote
space group	$P6_522$			
unit cell dimensions	$a = b = 76.22$ Å, $c = 146.93$ Å, $\alpha = \beta = 90°$, $\gamma = 120°$			
solvent content	69%			
X-ray source	X06SA (SLS)	ID23-1 (ESRF)		
detector	MAR-CCD225	ADSC Quantum Q210		
energy (keV)	12.3000	9.8825	9.6624	10.2000
resolution (Å)	18−1.9 (2.0−1.9)	15−3.35 (3.4−3.35)	15−3.45 (3.5−3.45)	15−3.5 (3.55−3.5)
no. of unique reflections/Bijvoets*	20520 (2851)	*33994 (1556)	*31059 (1347)	*29580 (1216)
R-factor (%)	7.1 (38.6)	11.1 (42.6)	10.6 (41.6)	12.9 (47.5)
multiplicity	10.4 (10.7)	3.9 (3.9)	3.7 (3.7)	3.9 (3.9)
completeness	99.7 (100.0)	98.8 (99.7)	98.2 (99.4)	98.2 (98.9)
$I/\sigma(I)$	20.7 (7.8)	9.8 (3.5)	10.1 (3.5)	9.2 (3.1)

no. of reflections in working/free set	19667/853
no. of protein chains	3
no. of protein residues/solvent atoms/zinc ions	139/158/6
R-factor/R_{free} (%)	19.9/25.2
rmsd for bond lengths (Å)/angles (deg)	0.012/1.35
Ramachandran plot, residues in disallowed regions	1 (Q44 in chain A)

following the protocol described above. This resulted in production of an insoluble sample, presumably due to the formation of $Zn_3(PO_4)_2$ sediments that depleted the medium of soluble zinc. Thus, refolding and purification protocols like those described for $B2^{C137D}$ were followed for all labeled samples used in NMR measurements.

NMR data were recorded at a sample concentration of 3 mM in 20 mM Tris (pH 7.0), 75 mM NaCl, and 10 mM β-mercaptoethanol. Protein backbone ^{15}N and ^{1}H resonances were assigned with ^{15}N-separated NOESY and TOCSY spectra. The oligomeric state of MuRF1 B2 was estimated from ^{1}H T_2 spin echo relaxation measurements as well as ^{15}N T_1, ^{15}N T_2, and ^{15}N heteronuclear NOE data. ^{15}N relaxation data were analyzed with TENSOR (*25*). RDCs were measured in a solution of 1 mM protein dissolved in 20 mM Tris (pH 7.0), 75 mM NaCl, and 10 mM β-mercaptoethanol supplemented with Pf1 phage (ASLA Biotech) (*26*) at a concentration of 15 mg/mL. The electrostatic alignment was tuned by addition of NaCl to a final concentration of 150 mM. Intersubunit NOEs to residue F148 were identified using a two-dimensional NOESY spectrum with a mixing time of 100 ms. Spectra were recorded on a BRUKER DRX 600 spectrometer equipped with a TXI probe and on a BRUKER DRX 800 spectrometer equipped with a TCI cryoprobe. Data were processed with NMRPipe (*27*) and analyzed with PIPP (*28*).

Multiangle Light Scattering Coupled to Size Exclusion Chromatography (SEC−MALS). Measurements were performed on an ÄKTA basic system (GE Healthcare) connected to a tri-angle light scattering detector and a differential refractometer (miniDAWN Tristar and Optilab, respectively). A Superdex 200 HR 10/300 GL column (GE Healthcare) was used in 50 mM Tris (pH 8.0) and 100 mM NaCl at a flow rate of 0.7 mL/min. Sample volumes of 100 μL were injected at a concentration of 2 mg/mL. A specific refractive index increment (d*n*/d*c*) value of 0.185 mL/g was used. The data were recorded and processed using ASTRA (Wyatt Technology). To determine the detector delay volumes and normalization coefficients for the MALS detector, a BSA sample (Sigma catalog no. A-8531) was used as a reference.

RESULTS AND DISCUSSION

Crystal Structure. The structure of human MuRF1 B2 has been elucidated by X-ray crystallography to 1.9 Å resolution (Figure 2a). The crystal form used in this study contains three molecular copies in its asymmetric unit that are nearly identical [average rmsd of 0.30 Å for 43 matching Cα atoms, calculated using SPDBV (*29*)]. Crystallographic data show that the B2 domain spans residues H119−L159 in MuRF1. It consists of a structural core formed by an α-helix (α1) that packs against a three-stranded antiparallel β-sheet (β1−β3), supporting three loop regions (L1, L2, and L3) involved in zinc binding, where L2 is, in fact, a conserved β-turn. Anomalous difference Fourier maps revealed that each molecular copy of B2 binds two zinc ions in cross-brace topology at a mutual distance of ∼10.7 Å, in agreement with inter-zinc distances observed in other B2 boxes (10.3−10.9 Å) (Figure 2b). Zinc-binding site ZnI involves residues C122xxH125 and C142xxC145, while site ZnII involves C134xxC137 and H151xxC154. The C-terminal cysteine ligand, C154, is a unique feature of human MuRF proteins. This residue is a conserved histidine in all other B2 boxes [52 sequences analyzed (Figure S1 of the Supporting Information)]. Thus, MuRF1 B2 is a representative of the CHC_2C_2HC B2 subtype.

The crystal structure of the MuRF1 B2 monomer is in good agreement with NMR models of the B2 domains from ATDC (2CSV), TRIM39 (2DID), TRIM41 (2EGM), TRIM5 (2YRG), MID2 (2DJA), MID1 (*9*), and MuRF1 (2D8U) (Figure 2b). A more detailed comparison of the crystal and NMR structures of MuRF1 B2 is given in Figure S2 of the Supporting Information.

In the B2 motif, zinc is coordinated through highly conserved cysteine and histidine residues, with the exception of the fourth ligand (in site ZnII) that is broadly degenerated. This position is often occupied by an aspartate residue (31 occurrences in 52 sequences), but it can also host a cysteine (16 of 52), a glutamate (3 of 52), a histidine (1 of 52), or a serine (1 of 52) (Figure S1 of the Supporting Information). All models of B2 boxes elucidated to date display regular aspartates in this location, with the exception of MuRF1 B2

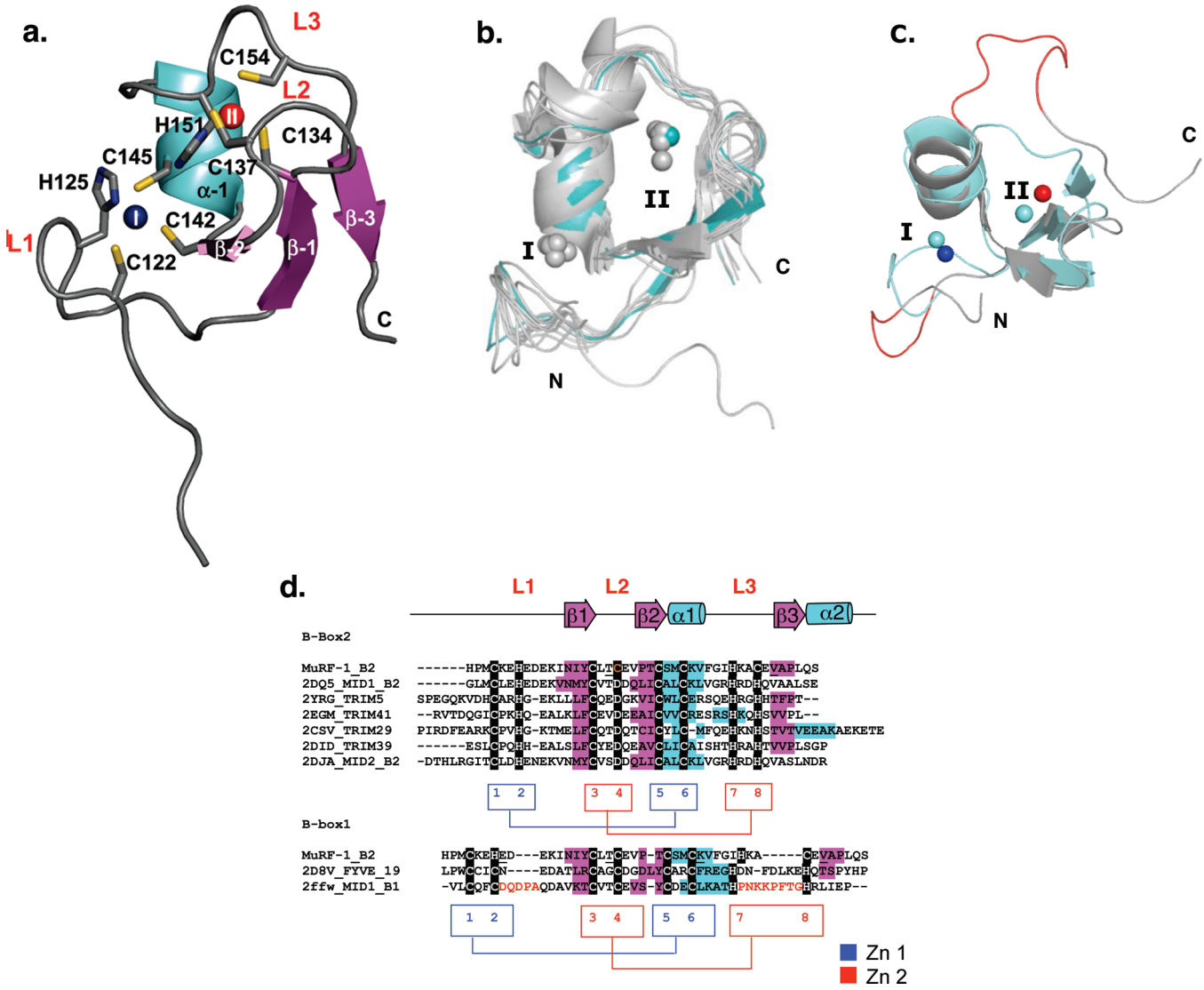

FIGURE 2: Structural characterization of B-boxes. (a) Crystal structure of MuRF1 B2. Metal binding ligands are displayed. The N- and C-terminal zinc ions are colored blue and red, respectively. Secondary structure elements and loops are labeled. (b) Superposition of B2 structures available to date, where MuRF1 B2 is highlighted in cyan. (c) Superposition of MuRF1 B2 (cyan) and MID1 B1 (gray), where loop insertions in the B1 family are colored red. (d) Structure-based sequence alignment of B-boxes with known structure. Secondary structure elements and loop regions are colored as in panel a. Metal ligands are highlighted in black, numbered, and colored according to the metal site they form. The mutated cysteine residue in the B^{C137D} variant is colored orange. The cross-brace topology is sketched.

that contains a cysteine. To investigate whether aspartate and cysteine ligands are interchangeable at this position, we analyzed a C137D mutated variant of MuRF1 B2 ($B2^{C137D}$). Comparative ^{1}H NMR measurements showed that both wild-type B2 and $B2^{C137D}$ shared a high degree of spectral similarity, indicative of common structural features. This was confirmed by a subsequent crystallographic analysis of $B2^{C137D}$, which demonstrated that the amino acid substitution neither influences the fold nor alters its zinc binding properties.

MuRF1 B2 Has a Dimeric Structure. The crystal structure of MuRF1 B2 reveals a dimer, where the α1 helix of one protomer docks into a concave depression formed by the α-helix and β-sheet of the other subunit (Figure 3b). The interface, which comprises an area of 515 Å^2 (calculated using the PISA server), contains clusters of hydrophobic and polar interactions (Figure 3c). Hydrophobic interactions involve residues M144 and F148 in helix α1 of one subunit and residues I132′ in strand β1 and 156′-VAP-158′ in strand β3 of the other subunit. Polar contacts are established by residues E128−N131′ and by the mutual packing of residue S143 from both α1 helices. Electron density maps for interface groups are shown in Figure S3 of the Supporting Information.

The groups involved in dimer formation in MuRF1 B2 are relatively well conserved within the B2 family (Figure S1 of the Supporting Information), in particular the hydrophobic groups in strands β1 and β3 and helix α1. Remarkably, positions S143 and F148 are subject to compensatory sequence variations, where position 143 commonly hosts a hydrophobic group and position 148 is most frequently a serine. The L1 loop also shows a propensity to host charged residues that could form interactions across protomers equivalent to those of MuRF1 B2, although a pattern of conservation is not detected. Thus, one might speculate that other B2 boxes could also dimerize following the pattern of MuRF1 B2. In contrast, B1 boxes seem to be unlikely to adopt this dimerization model. As opposed to the short loops of B2 boxes, which are conserved in length, B1 boxes contain two long variable regions following the second and seventh

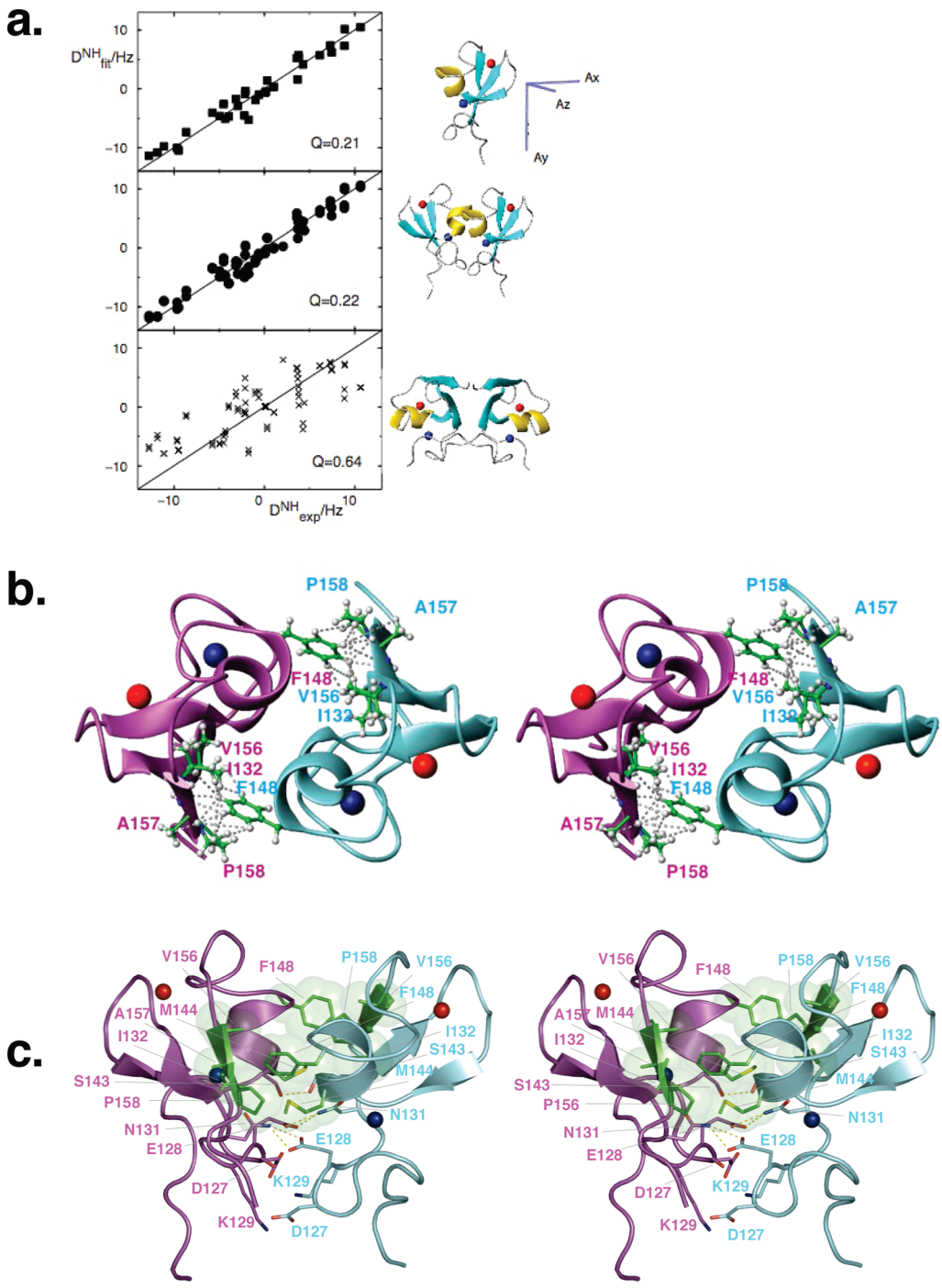

FIGURE 3: Dimeric structure of MuRF1 B2. (a) Fitting of $^{1}H-^{15}N$ RDC data to the crystal structures of the monomer (top), the dimer in the asymmetric unit (middle), and the dimer formed by crystallographic symmetry (bottom). (b) Stereo representation of intersubunit NOEs (15 in total; shown as dashed lines) measured between the protons of F148 and neighboring hydrophobic residues. (c) Stereoview of the interface contacts in the crystal structure of dimeric MuRF1 B2. Hydrophobic groups are colored green and highlighted using van der Waals spheres. Polar interactions are represented as dashed lines.

zinc ligands (*2*) (Figure 2c,d). In MID1 B1 (*12*), the C-terminal insertion adopts a bulky, "lasso-like" structure stabilized by conserved proline residues that can be expected to sterically prevent the formation of a dimeric arrangement like that of MuRF1 B2.

Oligomeric State in Solution. To establish the oligomeric state of MuRF1 B2 in solution, we analyzed it using analytical ultracentrifugation. Sedimentation equilibrium experiments confirmed the dimeric character of the domain and suggested a strong association constant (Figure 4a). Since the sample remained predominantly dimeric at the lowest assayed concentration of 4.8 μM, we concluded that the dissociation constant of the interaction must be below that, possibly in the submicromolar range.

These conclusions were supported by NMR data obtained from ^{15}N-enriched samples. The correlation time (τ_c) at 25 °C derived from ^{1}H T_2 and a complete set of ^{15}N relaxation data (T_1, T_2, and $\{^{1}H\}-^{15}N$ NOEs) was 6.4 $\pm$ 0.1 ns, corresponding to a molecular mass (M_r) of ~12 kDa, approximately twice that of a B2 monomer (5.2 kDa). Experimental diffusion parameters and residue-specific relaxation properties are given in Table 1 and Figure S4 of

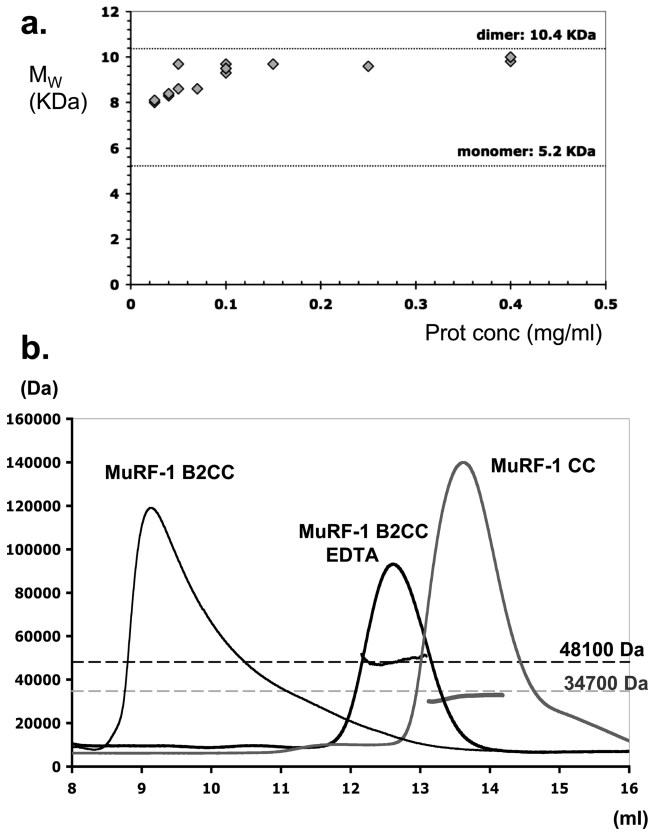

FIGURE 4: Oligomeric states of MuRF1 B2 and CC domains. (a) Molecular masses (M_r) of MuRF1 B2 calculated from sedimentation equilibrium measurements. (b) SEC−MALS measurements of MuRF1 CC and B2CC truncated variants. The average M_r per volume unit (dots) and the normalized refractive index (solid lines) are shown. The theoretical M_r values of the dimeric states of CC and B2CC constructs are represented as dashed horizontal lines. Unfolding of B2 in the B2CC variant was achieved by mixing with 50 mM EDTA and 10 mM β-mercaptoethanol for 16 h at 4 °C.

the Supporting Information. The stability of the dimer was confirmed by monitoring the sample through a dilution series [^{1}H−^{15}N HSQC spectra in the concentration range 3−0.3 mM and ^{1}H spectra for further dilutions down to 20 μM (Figures S5 and S6 of the Supporting Information)]. In agreement with sedimentation equilibrium data, NMR spectra remained virtually unchanged at the concentrations that were tested, indicating that MuRF1 B2 retained its association state through the concentrations that were assayed. Equivalent results were obtained from the NMR analysis of B2^{C137D}, proving that the dimerization properties of this domain are independent of its zinc-binding ligands.

Validation of the Dimer Structure. To assess whether the dimer of MuRF1 B2 in the crystalline state corresponds to that in solution, ^{1}H−^{1}H NOE and ^{15}N−^{1}H residual dipolar couplings (RDCs) recorded from weakly aligned samples in a medium containing Pf1 phage were compared to all possible structural models derived from the crystal lattice, namely, (i) the monomer, (ii) the dimer in the asymmetric unit (described above), and (iii) one additional dimeric form that arises in the lattice by crystallographic symmetry (Figure 3a). A description of the lattice of this crystal form is given in Figure S7 of the Supporting Information. The NMR data (Figure S8 of the Supporting Information) revealed 15 NOEs between the H$^\delta$ and H$^\epsilon$ ring protons of residue F148 and the cluster formed by I132, V156, A157, and P158. These are perfectly satisfied by dimer ii as short intermolecular contacts (<5 Å) (Table S1 of the Supporting Information and Figure 3b) but cannot be satisfied within the monomeric structure (i) or the lattice dimer (iii) [in which the respective proton distances are >10 Å (Table S1 of the Supporting Information)]. It should be noted that dimer ii, but not dimer iii, has its termini arranged in parallel and is consistent with the known composition of the TRIM fold where the B2 box is followed by a parallel coiled coil domain.

This result was in agreement with a subsequent analysis based on RDC data (Figure S9 of the Supporting Information), where alignment tensors were obtained by fitting the RDCs to the respective coordinates (models i−iii) (Figure 3a). In the case of dimeric structures, dipolar couplings for the equivalent internuclear vectors in both protomers are averaged. Thus, one of the principal axes of the alignment tensors for dimers must coincide with the dimer C_2 axis, and monomeric and dimeric forms cannot be distinguished on the basis of the fitting of RDCs to coordinates alone. The RDC data showed excellent agreement with the tertiary structure of the monomer (i) in the crystal ($Q = 0.21$; Q-factor definition as in ref *30*), confirming that the crystal structure of the MuRF1 B2 protomer represents closely the protein in solution. The fitting of RDCs to the noncrystallographic dimer ii yielded an agreement ($Q = 0.22$) similar to that of the monomer, which is expected if the internal symmetry of the dimer in the crystal is identical to that in solution. In contrast, lattice dimer iii fitted the data poorly ($Q = 0.64$), which rules out the existence of this form in solution. Thus, both NOE and RDC data corroborated the initial expectation that the dimer revealed by the crystal structure coincides with that present in solution.

Distinct Dimerization Pattern. The dimeric arrangement of MuRF1 B2 is different from that of other RING-like domains (Figure 5). Even though the dimerization modes of RING folds are highly heterogeneous, involving different secondary structure elements and sequence groups, some general patterns can be observed. The RING finger of RAG1 (*31*), the heterodimeric BRCA1−BARD1 tumor suppressor (*32*), the homodimeric FYVE domain from EEA1 (*33*) and the U-box of CHIP (*34, 35*) self-assemble via additional α-helical extensions. In those cases where direct contacts across the zinc-binding motifs are present, as in the Hdm2 RING (*36*) and the Prp19 U-box (*37*), these commonly involve the β-sheet component and/or its neighboring loop region. Helix α1 invariably lies in the outside, opposite to the dimer interface. A similar arrangement is also observed in the tandem interaction of boxes B1 and B2 in MID1 (*38*). By comparison, the MuRF1 B2 dimer could be regarded as having a "reverse" geometry. Furthermore, in the absence of additional helical extensions [with the exception of Hdm2 RING (*36*)], the self-association of other motifs appears weak (*37*), while the dimerization of MuRF1 B2 is stable and occurs at low concentrations. This suggests that the B2 box might contribute to the overall assembly of MuRF1.

Contribution of B2 and CC Domains to MuRF1 Quaternary Structure. MuRF1 contains a dimeric CC motif C-terminal to its B2 box (*14*). To investigate how the dimerization properties of the B2 motif relate to those imposed on MuRF1 by its CC domain, we compared the M_r values of two MuRF1 variants corresponding to the isolated

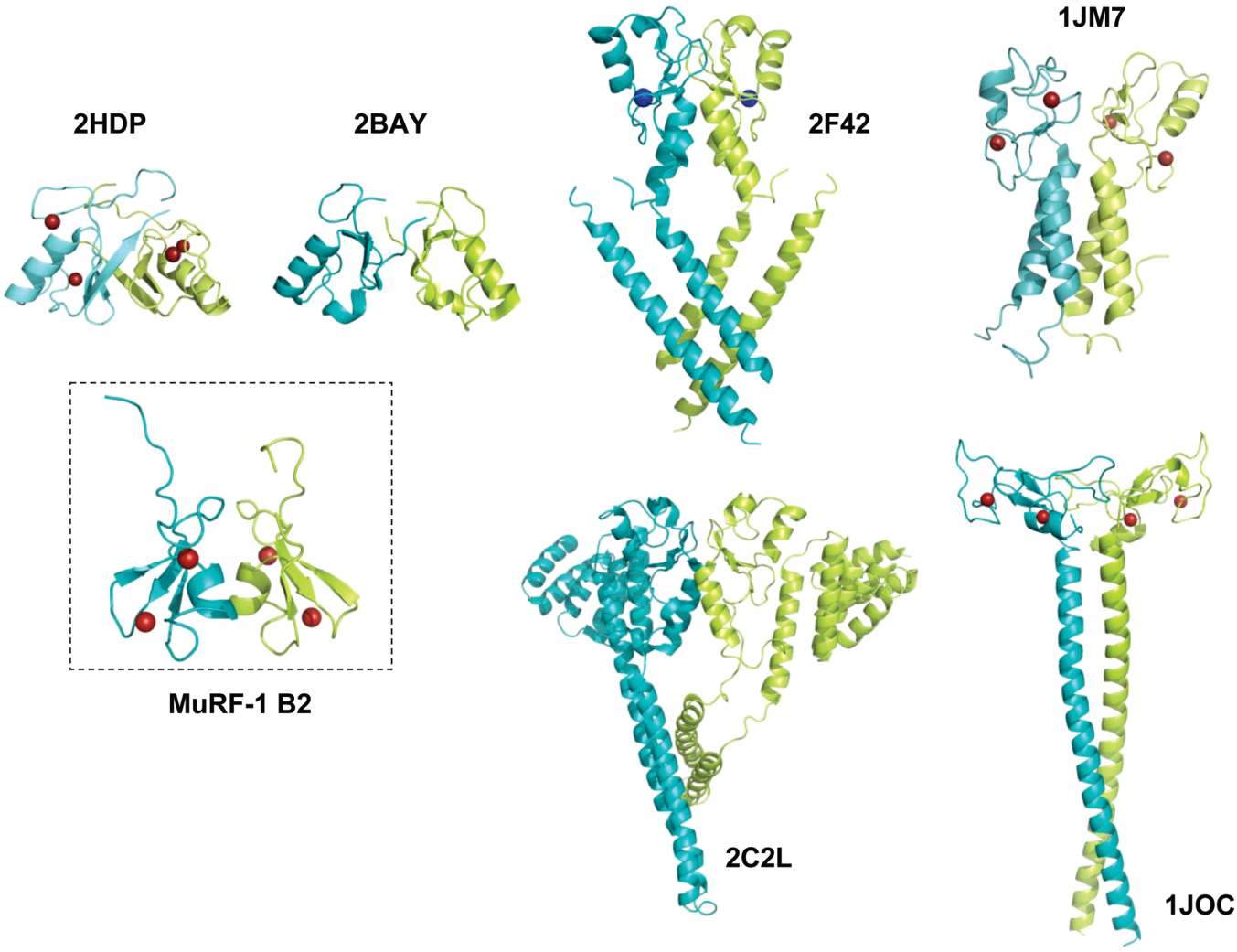

FIGURE 5: Dimeric structure of RING-like motifs. Structures correspond to the Hdm2 RING domain (2HDP), the U-box (2BAY), dimerization and U-box domains of CHIP (2F42), the BRCA1−BARD1 heterodimer (1JM7), the CHIP−Ubc13−Uev1a complex (2C2L), and the EEA1 homodimer (1JOC).

CC motif (MuRF1 CC) and the B2 box followed by the CC motif (MuRF1 B2CC) (construct definition as in Figure 1) using multiangle light scattering coupled to size exclusion chromatography (SEC−MALS) (Figure 4b). The data showed that MuRF1 CC forms dimers as main species in solution but that the presence of B2 in the B2CC variant leads to the formation of higher-order oligomeric species. Even though the polydispersity of the resulting assemblies did not allow calculation of their M_r accurately, this could be approximated to that of hexameric or octameric formations. To verify that the increased level of assembly in B2CC was due to the presence of the B2 box, a B2CC sample in which the B2 had been unfolded by metal depletion (using EDTA) was assayed. The latter formed exclusively dimers mediated by the intact CC fraction (Figure 4b), proving that B2 induces a high-order association. Clearly, the oligomeric state of full-length MuRF1 must become known before the physiological relevance of the B2-induced higher-order assembly can be established. Nonetheless, it is worth noting that these findings correlate with the evolutionary invariability of the B2 domain directly preceding the CC region, which suggests that the B2CC fraction might act as an integrated module in securing the correct quaternary structure of the TRIM fold.

Surface Features. To reveal the possible determinants of protein interaction in MuRF1 B2, we examined its surface topography. Each protomer exhibits a long, shallow groove that encircles the C-terminal metal site ZnII formed by loops L2 and L3. The groove comprises a hydrophobic cluster contributed by the solvent-exposed surface of the β-sheet that includes the highly conserved aromatic residue Y133. This groove does not resemble those defining ubiquitin ligase activity in RING domains (*34*), suggesting that this B2 box is unlikely to be involved in ubiquitination. Instead, one might speculate that the hydrophobic features of this groove, which are conserved in B2 sequences, might mediate the heterologous interactions established by this motif. These conclusions concur with those obtained from MID1 B2, whose role in ubiquitination was also thought to be unlikely and whose hydrophobic surface area was suggested as possible mediators of protein interactions (*9*). Potentially, this feature of the B2 motif might provide specificity when strategies for attempting the therapeutic targeting of TRIM proteins are designed.

Comparative Overview. The B-box fold belongs to the RING finger superfamily of zinc-binding motifs, which comprises RING (*39*), PHD (*40*), FYVE (*41*), ZZ (*42*), U-box (*43*), and B-boxes B1 (*8*) and B2. These folds,

although poorly related in sequence and loop structure, share a common $\beta\beta\alpha$ core that supports the ligation of two zinc ions in a cross-brace fashion (Figure S10 of the Supporting Information) [with the exception of the U-box domain that does not bind zinc but, instead, exhibits a network of hydrogen bonds and salt bridges (*43*)]. The different folds become individualized through the nature of their conserved zinc binders and the length and composition of the spacing sequences, which confer them substantial structural plasticity and allow a broad range of protein interactions and cellular roles to be supported. The B2 box is the most compact of these folds. The short sequences between its metal binders result in an inter-zinc distance of ~10.7 Å, similar to that of the FYVE motif, but shorter than that of ZZ and B1 boxes (~13 Å) and RING and PHD domains (~14 Å). Conserved hydrophobic residues within the respective RING folds mediate the packing of the β-sheet against the α-helix and are primarily located around the fifth metal ligand, in the segment connecting strand β2 to helix α1 (Figure S10 of the Supporting Information). Interestingly, the hydrophobic residues of MuRF1 B2 in this position do not form a motif core but are part of its dimerization interface. In fact, MuRF1 B2 does not have a defined hydrophobic core beyond the interaction of V156 with the aliphatic chain of K146, indicating that it is mostly stabilized by metal binding and self-assembly.

The α/β core of RING folds is most structurally similar at metal site ZnI, while the loops and metal ligands around C-terminal site ZnII display significant variability, both within and across families (Figure S10 of the Supporting Information). Also in the B2 group, variations accumulate around ZnII. All structures available to date correspond to the predominant $CHCDC_2H_2$ form, while MuRF1 B2 is the only representative of a CHC_2C_2HC variant. The difference in metal binders, however, does not translate into noticeable structural differences in the family, which forms a closely related structural group (Figure 2b). Finally, MuRF1 B2 is to serve as a close representative of the B2 domains of the MuRF2 and MuRF3 members of the MuRF family. Since this box contains unique structural features in contrast to other RING-like folds, it might provide specificity for the therapeutical targeting of MuRF1. In this respect, future studies of the molecular interactions established by this B2 domain will shed light on its cellular role and potential pharmacological relevance.

ACKNOWLEDGMENT

Special thanks go to the staff at beamlines ID23-1 (ESRF, Grenoble, France) and X06SA (SLS, Villigen, Switzerland) for support during data collection.

SUPPORTING INFORMATION AVAILABLE

Interproton distances within the MuRF1 B2 monomer and its possible dimeric states in the crystallographic lattice (Table S1), alignment of B2 sequences (Figure S1), comparison of crystallographic and NMR models of MuRF1 B2 (Figure S2), views of the $(2F_{obs} - F_{calc})\alpha_{calc}$ electron density map (Figure S3), NMR relaxation data (Figure S4), assigned HSQC NMR spectrum (Figure S5), comparative HSQC data for diluted B2 samples (Figure S6), description of dimeric formations in the crystalline lattice (Figure S7), NOE data (Figure S8), RDC data (Figure S9), and a comparative overview of RING-like motifs (Figure S10).

This material is available free of charge via the Internet at http://pubs.acs.org.

REFERENCES

1. Meroni, G., and Diez-Roux, G. (2005) TRIM/RBCC, a novel class of 'single protein RING finger' E3 ubiquitin ligases. *BioEssays 27*, 1147–1157.
2. Short, K. M., and Cox, T. C. (2006) Subclassification of the RBCC/TRIM superfamily reveals a novel motif necessary for microtubule binding. *J. Biol. Chem. 281*, 8970–8980.
3. Reymond, A., Meroni, G., Fantozzi, A., Merla, G., Cairo, S., Luzi, L., Riganelli, D., Zanaria, E., Messali, S., Cainarca, S., Guffanti, A., Minucci, S., Pelicci, P. G., and Ballabio, A. (2001) The tripartite motif family identifies cell compartments. *EMBO J. 20*, 2140–2151.
4. Torok, M., and Etkin, L. D. (2001) Two B or not two B? Overview of the rapidly expanding B-box family of proteins. *Differentiation 67*, 63–71.
5. Shoham, N., Cohen, L., Gazit, A., and Yaniv, A. (2003) The Tat protein of the caprine arthritis encephalitis virus interacts with the Notch2 EGF-like repeats and the epithelin/granulin precursor. *Intervirology 46*, 239–244.
6. Short, K. M., Hopwood, B., Yi, Z., and Cox, T. C. (2002) MID1 and MID2 homo- and heterodimerise to tether the rapamycin-sensitive PP2A regulatory subunit, α4, to microtubules: Implications for the clinical variability of X-linked Opitz GBBB syndrome and other developmental disorders. *BMC Cell Biol. 3*, 1–6.
7. Peng, H., Begg, G. E., Harper, S. L., Friedman, J. R., Speicher, D. W., and Rauscher, F. J., III (2000) Biochemical analysis of the Kruppel-associated box (KRAB) transcriptional repression domain. *J. Biol. Chem. 275*, 18000–18010.
8. Massiah, M. A., Simmons, B. N., Short, K. M., and Cox, T. C. (2006) Solution structure of the RBCC/TRIM B-box1 domain of human MID1: B-box with a RING. *J. Mol. Biol. 358*, 532–545.
9. Massiah, M. A., Matts, J. A., Short, K. M., Simmons, B. N., Singireddy, S., Yi, Z., and Cox, T. C. (2007) Solution structure of the MID1 B-box2 $CHC(D/C)C_2H_2$ zinc-binding domain: Insights into an evolutionarily conserved RING fold. *J. Mol. Biol. 369*, 1–10.
10. Borden, K. L., Lally, J. M., Martin, S. R., O'Reilly, N. J., Etkin, L. D., and Freemont, P. S. (1995) Novel topology of a zinc-binding domain from a protein involved in regulating early *Xenopus* development. *EMBO J. 14*, 5947–5956.
11. Bodine, S. C., Latres, E., Baumhueter, S., Lai, V. K., Nunez, L., Clarke, B. A., Poueymirou, W. T., Panaro, F. J., Na, E., Dharmarajan, K., Pan, Z. Q., Valenzuela, D. M., DeChiara, T. M., Stitt, T. N., Yancopoulos, G. D., and Glass, D. J. (2001) Identification of ubiquitin ligases required for skeletal muscle atrophy. *Science 294*, 1704–1708.
12. Witt, C. C., Witt, S. H., Lerche, S., Labeit, D., Back, W., and Labeit, S. (2008) Cooperative control of striated muscle mass and metabolism by MuRF1 and MuRF2. *EMBO J. 27*, 350–360.
13. Centner, T., Yano, J., Kimura, E., McElhinny, A. S., Pelin, K., Witt, C. C., Bang, M. L., Trombitas, K., Granzier, H., Gregorio, C. C., Sorimachi, H., and Labeit, S. (2001) Identification of muscle specific ring finger proteins as potential regulators of the titin kinase domain. *J. Mol. Biol. 306*, 717–726.
14. Mrosek, M., Labeit, D., Witt, S., Heerklotz, H., von Castelmur, E., Labeit, S., and Mayans, O. (2007) Molecular determinants for the recruitment of the ubiquitin-ligase MuRF1 onto M-line titin. *FASEB J. 21*, 1383–1392.
15. McElhinny, A. S., Kakinuma, K., Sorimachi, H., Labeit, S., and Gregorio, C. C. (2002) MuRF1 interacts with titin to regulate sarcomeric M-line and thick filament structure and may have nuclear functions via its interaction with glucocorticoid modulatory element binding protein-1. *J. Cell Biol. 157*, 125–136.
16. Koyama, S., Hata, S., Witt, C. C., Ono, Y., Lerche, S., Ojima, K., Chiba, T., Doi, N., Kitamura, F., Tanaka, K., Abe, K., Witt, S. H., Rybin, V., Gasch, A., Franz, T., Labeit, S., and Sorimachi, H. (2008) Muscle RING-finger protein-1 (MuRF1) as a connector of muscle energy metabolism and protein synthesis. *J. Mol. Biol. 376*, 1224–1236.
17. Kabsch, W. (1993) Automatic processing of rotation diffraction data from crystals of initially unknown symmetry and cell constants. *J. Appl. Crystallogr. 26*, 795–800.

18. Terwilliger, T. C., and Berendzen, J. (1999) Automated MAD and MIR structure solution. *Acta Crystallogr. D55*, 849–861.
19. Terwilliger, T. C. (2002) Automated main-chain model-building by template-matching and iterative fragment extension. *Acta Crystallogr. D59*, 34–44.
20. Perrakis, A., Morris, R. M., and Lamzin, V. S. (1999) Automated protein model building combined with iterative structure refinement. *Nat. Struct. Biol. 6*, 458–463.
21. Jones, T. A., Zou, J. Y., Cowan, S. W., and Kjeldgaard, M. (1991) Improved methods for building protein models in electron density maps and the location of errors in these models. *Acta Crystallogr. A47*, 110–119.
22. Adams, P. D., Grosse-Kunstleve, R. W., Hung, L. W., Ioerger, T. R., McCoy, A. J., Moriarty, N. W., Read, R. J., Sacchettini, J. C., Sauter, N. K., and Terwilliger, T. C. (2002) PHENIX: Building new software for automated crystallographic structure determination. *Acta Crystallogr. D58*, 1948–1954.
23. Storoni, L. C., McCoy, A. J., and Read, R. J. (2004) Likelihood-enhanced fast rotation functions. *Acta Crystallogr. D60*, 432–438.
24. Machaidze, G., and Lustig, A. (2006) SEGAL, a semi-automatic program for fitting sedimentation equilibrium patterns from analytical ultracentrifugation. *J. Biol. Phys. Chem. 6*, 91–102.
25. Dosset, P., Hus, J. C., Blackledge, M., and Marion, D. (2000) Efficient analysis of macromolecular rotational diffusion from heteronuclear relaxation data. *J. Biomol. NMR 16*, 23–28.
26. Hansen, M. R., Mueller, L., and Pardi, A. (1998) Tunable alignment of macromolecules by filamentous phage yields dipolar coupling interactions. *Nat. Struct. Biol. 5*, 1065–1074.
27. Delaglio, F., Grzesiek, S., Vuister, G. W., Zhu, G., Pfeifer, J., and Bax, A. (1995) Nmrpipe: A Multidimensional Spectral Processing System Based on Unix Pipes. *J. Biomol. NMR 6*, 277–293.
28. Garrett, D. S., Powers, R., Gronenborn, A. M., and Clore, G. M. (1991) A Common-Sense Approach to Peak Picking in 2D, 3D, and 4D Spectra Using Automatic Computer-Analysis of Contour Diagrams. *J. Magn. Reson. 95*, 214–220.
29. Guex, N., and Peitsch, M. C. (1997) SWISS-MODEL and the Swiss-PdbViewer: An environment for comparative protein modeling. *Electrophoresis 18*, 2714–2723.
30. Cornilescu, G., Marquardt, J. L., Ottiger, M., and Bax, A. (1998) Validation of protein structure from anisotropic carbonyl chemical shifts in a dilute liquid crystalline phase. *J. Am. Chem. Soc. 120*, 6836–6837.
31. Bellon, S. F., Rodgers, K. K., Schatz, D. G., Coleman, J. E., and Steitz, T. A. (1997) Crystal structure of the RAG1 dimerization domain reveals multiple zinc-binding motifs including a novel zinc binuclear cluster. *Nat. Struct. Biol. 4*, 586–591.
32. Brzovic, P. S., Rajagopal, P., Hoyt, D. W., King, M. C., and Klevit, R. E. (2001) Structure of a BRCA1-BARD1 heterodimeric RING-RING complex. *Nat. Struct. Biol. 8*, 833–837.
33. Dumas, J. J., Merithew, E., Sudharshan, E., Rajamani, D., Hayes, S., Lawe, D., Corvera, S., and Lambright, D. G. (2001) Multivalent endosome targeting by homodimeric EEA1. *Mol. Cell 8*, 947–958.
34. Zheng, N., Wang, P., Jeffrey, P. D., and Pavletich, N. P. (2000) Structure of a c-Cbl-UbcH7 complex: RING domain function in ubiquitin-protein ligases. *Cell 102*, 533–539.
35. Xu, Z., Devlin, K. I., Ford, M. G., Nix, J. C., Qin, J., and Misra, S. (2006) Structure and interactions of the helical and U-box domains of CHIP, the C terminus of HSP70 interacting protein. *Biochemistry 45*, 4749–4759.
36. Kostic, M., Matt, T., Martinez-Yamout, M. A., Dyson, H. J., and Wright, P. E. (2006) Solution structure of the Hdm2 C2H2C4 RING, a domain critical for ubiquitination of p53. *J. Mol. Biol. 363*, 433–450.
37. Vander Kooi, C. W., Ohi, M. D., Rosenberg, J. A., Oldham, M. L., Newcomer, M. E., Gould, K. L., and Chazin, W. J. (2006) The Prp19 U-box Crystal Structure Suggests a Common Dimeric Architecture for a Class of Oligomeric E3 Ubiquitin Ligases. *Biochemistry 45*, 121–130.
38. Tao, H., Simmons, B. N., Singireddy, S., Jakkidi, M., Short, K. M., Cox, T. C., and Massiah, M. A. (2008) Structure of the MID1 tandem B-boxes reveals an interaction reminiscent of intermolecular ring heterodimers. *Biochemistry 47*, 2450–2457.
39. Barlow, P. N., Luisi, B., Milner, A., Elliott, M., and Everett, R. (1994) Structure of the C3HC4 domain by ^{1}H-nuclear magnetic resonance spectroscopy. A new structural class of zinc-finger. *J. Mol. Biol. 237*, 201–211.
40. Capili, A. D., Schultz, D. C., Rauscher, I. F., and Borden, K. L. (2001) Solution structure of the PHD domain from the KAP-1 corepressor: Structural determinants for PHD, RING and LIM zinc-binding domains. *EMBO J. 20*, 165–177.
41. Misra, S., and Hurley, J. H. (1999) Crystal structure of a phosphatidylinositol 3-phosphate-specific membrane-targeting motif, the FYVE domain of Vps27p. *Cell 97*, 657–666.
42. Legge, G. B., Martinez-Yamout, M. A., Hambly, D. M., Trinh, T., Lee, B. M., Dyson, H. J., and Wright, P. E. (2004) ZZ domain of CBP: An unusual zinc finger fold in a protein interaction module. *J. Mol. Biol. 343*, 1081–1093.
43. Ohi, M. D., Vander Kooi, C. W., Rosenberg, J. A., Chazin, W. J., and Gould, K. L. (2003) Structural insights into the U-box, a domain associated with multi-ubiquitination. *Nat. Struct. Biol. 10*, 250–255.

BI800733Z